Power Electronic Systems
Laboratory

IEEE/ASME Transactions onMechatronics, Vol. 17, No. 6, pp. 1088-1097, December 2012.

Motor Torque and Magnetic Levitation Force Generation in Bearingless Brushless Multipole Motors

F. Zürcher
T. Nussbaumer
J. W. Kolar

Eidgenössische Technische Hochschule Zürich
Swiss Federal Institute of Technology Zurich

Motor Torque and Magnetic Levitation Force Generation in Bearingless Brushless Multipole Motors

Franz Zürcher, *Student Member, IEEE*, Thomas Nussbaumer, *Member, IEEE*, and Johann W. Kolar, *Fellow, IEEE*

***Abstract*—In this paper, the principles of motor torque and suspension force generation in bearingless brushless motors with high pole numbers are explained, graphically illustrated, and analyzed in detail. The necessary harmonic components of the flux density distribution in the air gap are calculated and it is visualized how these can be generated by superposition of harmonics depending on a specific rotor pole/stator slot ratio. Especially, for bearingless motors with a fractional pole/slot ratio, it is shown how superior and precise suspension performance and high rotational speeds can be achieved. A basic analytical model is introduced and the considerations are exemplified for a 26-pole/24-slot bearingless brushless single-layer motor with concentrated windings compared to alternative feasible configurations. Adequate performance criteria for the motor as well as the bearing comparison are defined.**

***Index Terms*—Brushless motors, finite elements methods, magnetic levitation, mathematical analysis, permanent-magnet motors, servomotors.**

I. Introduction

THE popularity of permanent-magnet bearingless brushless motors is constantly increasing in a broad band of applications [1]. In bearingless motors, the six degrees of freedom of the levitated rotor are controlled precisely by magnetic forces. Since no lubricants are needed and no wear caused by friction is occurring, they need only very little maintenance, which make them suitable for applications such as vacuum and fluid pumps in chemical, pharmaceutical, and semiconductor industries. Additionally, bearingless motors are dedicated in applications under extreme conditions like, for example, satellite technology in outer space [1], [2], where any lubricants would evaporate due to the vacuum. Also in biochemical and medical applications [3]–[5], where an ultrahigh cleanness has to be guaranteed, bearingless motors offer valuable advantages. Flywheels for energy storage [6], as a further example, benefit from reduced friction losses by using magnetic bearings. In all these mentioned applications, bearingless motors are profitable in spite of their higher costs and system complexity compared to classical mechanical bearings. All the mentioned applications have in common that the requirements concerning the preciseness of the magnetic actuators (i.e., the electromagnets) and the position sensors are particularly high.

Different concepts for magnetic bearings [7]–[9] and bearingless motors [10]–[15] have been proposed so far, whereby for most of the aforementioned applications a very promising concept is the bearingless brushless slice motor as proposed in [16] and [17] due to its superior performance results. Thanks to its passive stabilization of the axial displacement and tilting, a highly compact setup can be achieved. For large rotor dimensions, this concept can be realized by a high number of rotor poles $2{\cdot}p$ combined with a fractional ratio of the number of stator slots q and rotor poles [18]. While the motor torque is generated by a sinusoidal air-gap flux distribution f_{drv} with a frequency component at

$$f_{\mathrm{drv}} = f_{\mathrm{mech}} \cdot p \tag{1}$$

where f_{mech} is the mechanical rotating speed, a resulting suspension force can be generated by an air-gap flux-density distribution f_{bng}, which exhibits a frequency component at

$$f_{\mathrm{bng}} = f_{\mathrm{mech}} \cdot (p \pm 1) \tag{2}$$

as described in [19]. These flux-density components can be generated by a suitable harmonic wave originating from the winding scheme in combination with the harmonics generated by the q-slotted stator teeth as will be shown in this paper.

The physical and mathematical principles of force and torque generation in this motor type are basically known and described in the literature. Different methods and models have been introduced to help to design and understand bearingless motors. Among others, magnetic reluctance models are introduced to calculate the magnetic circuits [14], [20], concepts known from control theory like transfer function characteristics are used to describe the bearing performance under different conditions [21], space vector modulation has been used to calculate the needed bearing currents [22], mathematical vector models [19] have been introduced to describe the occurring force components acting on the rotor, and of course various simulation techniques such as 2-D- or 3-D-finite element method (FEM) simulations have been used to investigate the behavior of bearingless motors [14]. In [1], an overview of activities of different institutions doing research on magnetic bearings is presented. However, a successful practical motor design is very hard to achieve based on the existing literature due to the high level of complexity associated with the bearingless motor concept. In particular, no illustrative explanation is given on how different

Manuscript received March 9, 2011; accepted May 30, 2011. Date of publication July 7, 2011; date of current version August 24, 2012. Recommended by Technical Editor H. Ding.

F. Zürcher and J. W. Kolar are with the Power Electronic Systems Laboratory, Swiss Federal Institute of Technology (ETH) Zürich, CH-8092 Zürich, Switzerland (e-mail: zurcher@ieee.org; kolar@lem.ee.ethz.ch).

T. Nussbaumer is with Levitronix GmbH, CH-8092 Zurich, Switzerland (e-mail: nussbaumer@levitronix.com).

Color versions of one or more of the figures in this paper are available online at http://ieeexplore.ieee.org.

Digital Object Identifier 10.1109/TMECH.2011.2159511

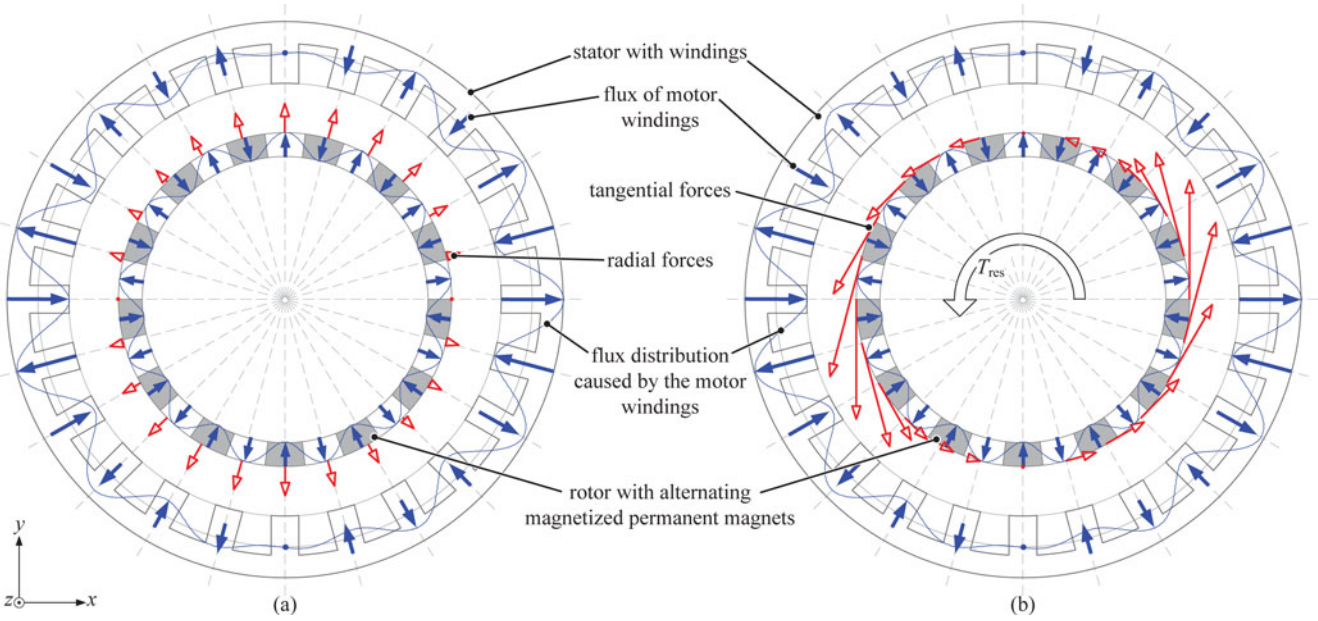

Fig. 1. Motor winding: the radial and tangential force components caused by the interaction of the air-gap flux density caused by the motor windings (blue line, drawn inside stator) and the rotor permanent magnets. While (a) radial force components cancel each other and thus no radial force is resulting, a resulting torque is generated by (a) tangential force components.

harmonics of the stator field and the rotor field may generate resulting radial suspension and tangential motor forces.

In this paper, an exemplary configuration with $2{\cdot}p = 26$ rotor poles, $q = 24$ stator slots, $m_{\mathrm{drv}} = 3$ motor drive phases as well as $m_{\mathrm{bng}} = 3$ bearing phases has been chosen, which is used to explain and visualize the principles. It is shown in a comprehensible manner how the magnetic field density distribution originating from a stator winding configuration placed in a certain number of stator slots may lead to a simultaneous suspension force and motor torque due to its interaction with the permanent-magnet rotor field. In particular, it will be shown analytically and graphically how the harmonics of the required fields are generated and how the radial suspension force and the motor torque can be controlled in an independent and decoupled manner by appropriate winding schemes.

In Section II, the force components that appear in bearingless motors by interaction of the permanent-magnet rotor field with the stator field will be explained and visualized for the exemplary configuration. In Section III, it will be shown how these force components can generate a resulting motor torque and suspension force. The generation of the required stator field by an appropriate winding configuration on the slotted stator will be discussed in Section IV. Section V gives a performance evaluation for different motor configurations and a guideline how to choose a rotor pole pair to stator slot combination to achieve a good motor and bearing performance. Finally, the findings are verified by 3-D FEM simulations and measurements on an exemplary prototype in Section VI.

II. Force Components in Bearingless Brushless Motors

For the sake of simplicity, only forces acting in the *xy*-plane of a cross section through the rotor and stator are considered in this paper. As long as the rotor is axially centered and not tilted about its x- or y-axis, the axial force components along the z-axis caused by edge effects do not contribute to the radial force and can, therefore, be ignored for the calculation of the levitation force. Here, the axial and tilting degrees of freedom of the rotor are assumed to be stabilized. This can be achieved by combining two bearingless motor units and an additional thrust bearing as proposed in [23] or alternatively by using an auxiliary passive bearing by having a slice-shaped or ring-shaped rotor such as introduced in [16]. The latter concept is called bearingless slice motor and is used for the prototype to verify the calculations in this paper. For this type of motor, the radial and tangential forces, which generate the motor torque and bearing force, can be calculated independently of the forces in the z-direction, as long as the rotor is neither deflected in the z-direction nor tilted about the x- or y-axes.

In order to understand and visualize the forces acting on the rotor of a bearingless motor, they can be divided into two components, namely a radial part F_{rad} and a tangential part F_{tan}, with respect to the outer rotor surface. Since the relative permeability of the stator iron teeth μ_{Fe} is very high compared to the relative permeability μ_0 in the air gap, only forces acting perpendicularly to the rotor- and stator-teeth surface are considered.

In Figs. 1 and 2, the radial and tangential force components resulting from the interaction of the sinusoidal rotor permanent-magnet field with the stator field, generated by the windings wound around the stator teeth, are shown for the exemplary configuration with $2{\cdot}p = 26$ and $q = 24$. Fig. 1 depicts the force components resulting from the motor windings, while Fig. 2 depicts the force components resulting from the bearing windings. Different components and their generation will be explained in the subsequent sections.

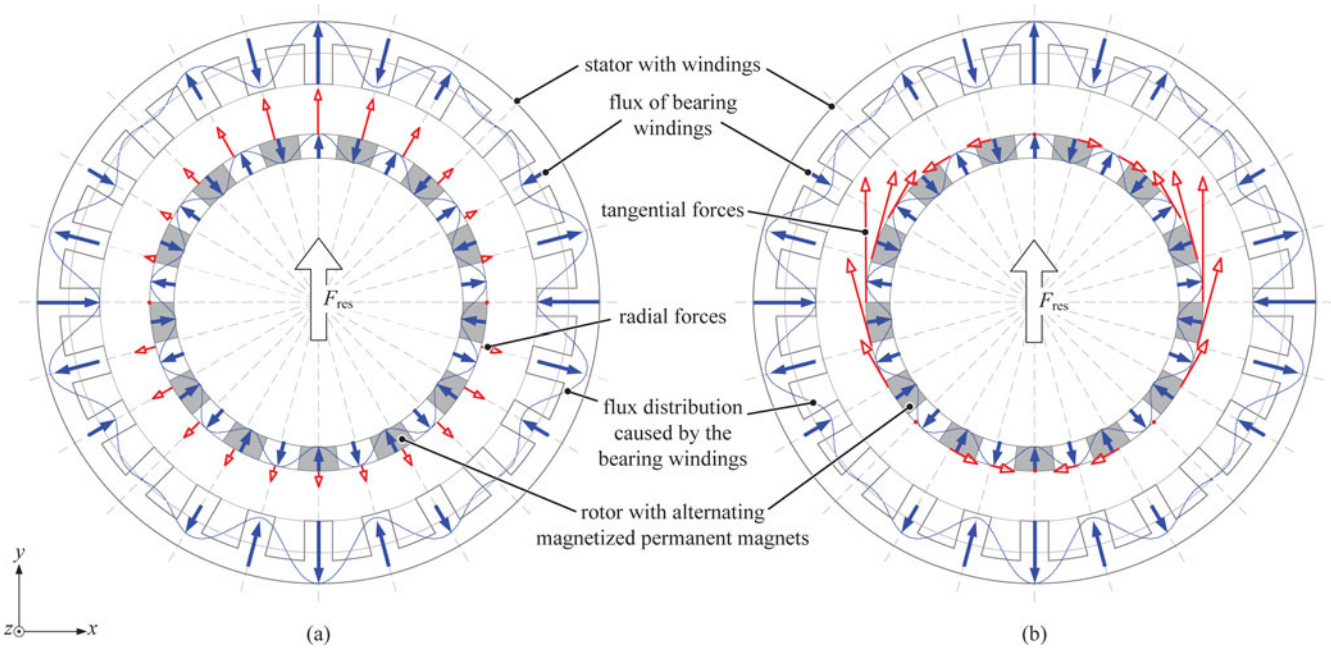

Fig. 2. Bearing winding: the radial and tangential force components caused by the interaction of the air-gap flux density caused by the bearing windings (blue line, drawn inside stator) and the permanent magnets. A resulting suspension force is generated by radial (a) force components as well as by (b) tangential force components, both pointing in the same direction.

A. Radial Force Components

The radial force components dF_{rad}, which are commonly denominated as Maxwell force components, are caused by the different relative permeabilities μ_0 of the air gap and μ_{Fe} of the stator iron. The magnitude of the components dF_{rad} is proportional to the square of the total magnetic flux density in the air gap, which is caused by the rotor permanent magnets and the additional flux density produced by the current flowing in the stator windings. Therefore, the radial force components dF_{rad} are always attracting the rotor to the stator teeth and only the magnitude can be influenced by an appropriate winding current. In a simplified sense, the components dF_{rad} can be calculated depending on the rotor angle φ according to

$$dF_{\mathrm{rad}} = \frac{\left(B_{\mathrm{pm}}(\varphi) + \Delta B_{\mathrm{wdg}}(\varphi)\right)^2 \cdot h \cdot r \cdot d\varphi}{2 \cdot \mu_0} \tag{3}$$

where the total magnetic flux density in the air gap consists of the flux density $B_{\mathrm{pm}}(\varphi)$ caused by the rotor permanent magnets and the flux density $\Delta B_{\mathrm{wdg}}(\varphi)$ caused by the currents in the stator windings, h is the rotor and stator heights, and r is the inner radius of the stator teeth.

As the radial Maxwell force components dF_{rad} always act perpendicularly to the rotor surface, they can never generate a torque on the rotor as can be seen in Figs. 1(a) and 2(a). But as will be seen later, they can be used to generate a resulting radial force, which is used for the bearingless levitation of the rotor as shown in Fig. 2(a).

B. Tangential Force Components

The tangential force components can be calculated by the formula known as the Lorentz force. According to [24], this formula can be applied despite the fact that the concentrated windings are placed in the stator slots, where virtually no permanent magnet field occurs. Instead, there are Maxwell force components, which act perpendicularly to the inner side of the stator teeth, and therefore generate a resulting lateral force on the rotor. In [24], it is shown that (4) can be used nevertheless and the virtual Lorentz force calculated in this manner is exactly equal to the sum of the real but small Lorentz force plus the lateral Maxwell force. Thus, the tangential force components dF_{tan} can simply be calculated according to

$$dF_{\mathrm{tan}} = \left(B_{\mathrm{pm}}(\varphi) \cdot dl_{\mathrm{wdg}}\right) \cdot I_{\mathrm{wdg}} \tag{4}$$

where $B_{\mathrm{pm}}(\varphi)$ is the radial flux caused by the rotor permanent magnets, dl_{wdg} is a length element of the windings in the magnetic field region, and I_{wdg} is the current flowing in the corresponding windings. As the magnitude of dF_{tan} is proportional to the winding current, tangential force components pointing in either clockwise or counterclockwise directions can easily be generated and controlled by applying a corresponding current in the windings.

The tangential force components can sum up to a resulting torque, as shown in Fig. 1(b), but they can also be used to generate a resulting suspension force if always the two opposite force components point in the opposite lateral direction as shown in Fig. 2(b).

III. Torque and Suspension Force Generation by Interaction of Harmonic Fields

A. Torque Generation by Tangential Force Components

In Fig. 1(b), it can be seen that the tangential force components according to (4) sum up to a resulting motor torque if the

order of the frequency component $f_{\mathrm{drv}}/f_{\mathrm{mech}}$ of the air-gap flux density distribution matches the number of the rotor pole-pairs p, which in the illustrated exemplary configuration is

$$\frac{f_{\mathrm{drv}}}{f_{\mathrm{mech}}} = p = 13. \tag{5}$$

Thus, a resulting torque is generated by the interaction of the two flux densities $B_{\mathrm{pm}}(\varphi)$ caused by the rotor permanent magnets and $B_{\mathrm{drv}}(\varphi)$ caused by the motor drive windings, both containing a frequency component with a significant magnitude at $f_{\mathrm{drv}} = f_{\mathrm{mech}} \cdot p$.

The radial force components calculated according to (3) can obviously never contribute to the motor torque, as they have no tangential part by definition. Also, the radial force components generated by the motor drive windings do not generate a resulting radial force on the rotor, as always the two opposite force components cancel each other out as can be seen in Fig. 1(a).

B. Suspension Force Generation by Tangential and Radial Force Components

By the bearing winding scheme, which is different from the motor drive winding scheme, an air-gap flux distribution with other frequency components is generated. In Section IV, it will be shown that a strong frequency component in this exemplary case occurs at

$$\frac{f_{\mathrm{bng}}}{f_{\mathrm{mech}}} = p + 1 = 14. \tag{6}$$

Since this fulfills (2), a resulting radial force is generated. In Fig. 2(a) and (b), it is visualized that both the radial Maxwell force components according to (3) and the tangential Lorentz force components according to (4) sum up to a resulting force, both pointing to the same direction. On the other hand, no torque is generated, as always two force components contribute with the same magnitude but different signs to the total torque, and thus cancel each other out.

If $p + 1$ in (6) would be replaced by $p - 1$, the two resulting forces in Fig. 2(a) and (b) would point to opposing directions and would partially cancel each other for interior rotor constructions.

IV. Generation of the Required Harmonic Stator Fields

As shown earlier, a motor torque can be generated by a sinusoidal stator flux-density distribution with $f_{\mathrm{drv}} = f_{\mathrm{mech}} \cdot p$, while a resulting suspension force can be generated by a flux-density distribution with a frequency component at $f_{\mathrm{bng}} = f_{\mathrm{mech}} \cdot (p \pm 1)$. These flux densities are generated by a suitable harmonic wave generated by an appropriate stator winding scheme and the harmonics generated by the q-slotted stator teeth.

For the calculation of the air-gap flux-density distribution resulting from the interacting fields of the rotor permanent-magnets flux and the flux caused by the stator windings, a simple model is introduced, which was verified by 3-D FEM simulations. According to the results, it can be used without loss of generality for the considered types of motors, whereby the flux density distribution caused by the radially magnetized rotor permanent magnets is supposed to be purely sinusoidal.

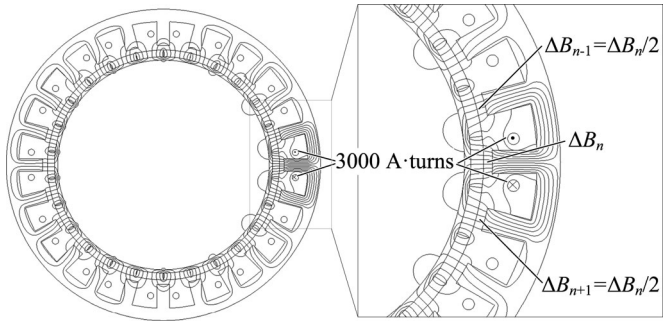

Fig. 3. 3-D FEM simulation results of the flux distribution of one single winding current with $I_{\mathrm{wdg}} = 3000$ A·turns, causing a flux difference ΔB_n in the air gap in front of the corresponding tooth.

A. Stator Winding Flux Distribution Model

The model, which was used to calculate the air-gap flux-density distribution, includes the following two simplifications.

1) The flux density ΔB_n in addition to the flux density $B_{\mathrm{pm}}(\varphi)$ caused by the permanent magnets in front of each stator tooth is assumed to be proportional to the current I_n flowing in the corresponding windings wound around this tooth.
2) The flux density in front of a tooth with no corresponding winding current is composed of half the negative sum of the flux densities of both of its direct neighbors, e.g., the flux density ΔB_n in front of the tooth i is equal to

$$\Delta B_n = \frac{(-\Delta B_{n-1}) + (-\Delta B_{n+1})}{2}. \tag{7}$$

This assumption can be made if only a small amount of the flux generated by the windings enters the rotor, which is typically the case for surface-mounted permanent-magnet motors with thin rotor iron thickness. Thus, the rotor iron is mostly saturated by the permanent-magnet flux whereby the flux of a winding returns mostly via its neighbored teeth. If the rotor iron was not saturated or the air gap was reduced to a smaller value and the relative permeability μ_r is assumed to be very high, the returning flux of a single tooth would be distributed equally to the other $q - 1$ stator teeth. In this case, the overall flux distribution would still have the same main harmonic components, although the motor as well as the bearing performance would be impaired since other frequency components occur, which do neither contribute to the motor torque nor to the bearing force. However, this effect is partially compensated by the higher overall flux density amplitude, due to the lower magnetic resistance of the nonsaturated iron.

For the calculations, in this paper the flux of a single winding is assumed to return only via the two direct neighbor teeth of the originating tooth. This fact has also been verified by 3-D FEM simulations for the exemplary configuration. Fig. 3 shows the flux distribution of a current $I_{\mathrm{wdg}} = 3000$ A·turns flowing in a single winding wound around one of the stator teeth. It can be seen that the winding current does not influence the air-gap flux

but the flux in front of the specific tooth and its direct neighbors. The flux in front of the other stator teeth is influenced only by the permanent magnets of the rotor. This allows a very easy way to calculate the stator flux density distribution.

B. Calculation of the Stator Flux Density Distribution

The total stator flux density is then calculated as a composition of two sine waves, a harmonic wave with order c_1 caused by the q-slotted stator teeth, and a wave c_2 generated by an appropriate winding scheme, which is different for the motor drive and bearing windings. As the motor drive and bearing teeth are split alternatingly, and thus only every second tooth is used for the motor drive or bearing winding, respectively, the order of c_1 is equal to $q/2$.

According to the well-known equation

$$\sin(\alpha)\cdot\sin(\beta)=\frac{\cos(\alpha-\beta)-\cos(\alpha+\beta)}{2} \tag{8}$$

the resulting flux density depending on the angle φ is proportional to

$$\begin{aligned}\Delta B(\varphi)&\sim\sin(c_1\cdot\varphi)\cdot\sin(c_2\cdot\varphi)\\&=\frac{\cos\left((c_1-c_2)\cdot\varphi\right)-\cos\left((c_1+c_2)\cdot\varphi\right)}{2}.\end{aligned} \tag{9}$$

Therefore, the resulting flux density exhibits harmonic components with the order $(c_1 - c_2)$ and $(c_1 + c_2)$. In the following, the harmonic flux density components will be calculated for the drive and the bearing system.

C. Motor Windings of the Exemplary Configuration

As explained in Section III-A, the required stator field for the generation of a motor torque must have the same number of poles $2{\cdot}p = 26$ as the rotor with its 26 permanent magnets. As mentioned earlier, this is achieved by the modulation of the harmonic wave with order $c_1 = q/2 = 12$ generated by the q stator slots and a sine wave with the order $c_{2,\mathrm{drv}} = 1$ generated by the appropriate drive winding scheme (cf., Table I for the winding scheme sequence.)

According to (9), the resulting stator flux density distribution $\Delta B_{\mathrm{drv}}(\varphi)$ of the motor drive windings along the circumferential angle φ is proportional to

$$\begin{aligned}\Delta B_{\mathrm{drv}}(\varphi)&\sim\sin(12\cdot\varphi)\cdot\sin(\varphi)\\&=\frac{\cos(11\cdot\varphi)-\cos(13\cdot\varphi)}{2}.\end{aligned} \tag{10}$$

Thus, the pth harmonic with $f_{\mathrm{drv}}/f_{\mathrm{mech}} = p = 13$ is generated. The flux in front of the active and passive stator teeth, generated by the drive windings, is depicted in Fig. 4(a). Interestingly, the 13th harmonic component of the resulting flux density is not directly visible. But a frequency analysis of the air-gap flux distribution [cf., Fig. 4(c)] shows that a frequency component with order $p = 13$ occurs as calculated earlier, which leads, by interaction with the rotor permanent magnets, to a resulting torque as shown in Fig. 1(b). Fig. 5(a) shows the resulting flux distribution of the drive windings together with the permanent magnets gained by 3-D FEM simulation. The tangential forces acting on the rotor and generating a resulting torque are visible.

TABLE I
WINDING CONFIGURATIONS FOR SOME EXEMPLARY SINGLE-LAYER AND THREE-PHASE MOTOR CONFIGURATIONS

$2{\cdot}p = 8$ and $q = 6$

1	**2**	**3**	**4**	**5**	**6**
D_1	$-B_1$	D_3	$-B_2$	D_2	$-B_3$

$2{\cdot}p = 14$ and $q = 12$

1	**2**	**3**	**4**	**5**	**6**	**7**	**8**	**9**	**10**	**11**	**12**
D_1	B_1	$-D_3$	B_3	D_2	B_2	$-D_1$	B_1	D_3	B_3	$-D_2$	B_2

$2{\cdot}p = 20$ and $q = 18$

1	**2**	**3**	**4**	**5**	**6**	**7**	**8**	**9**	**10**	**11**	**12**	**13**	**14**	**15**	**16**	**17**	**18**
D_1	B_1	D_1	$-B_3$	$-D_2$	$-B_1$	D_3	B_3	D_3	$-B_2$	$-D_1$	$-B_3$	D_2	B_2	D_2	$-B1$	$-D3$	$-B_2$

$2{\cdot}p = 26$ and $q = 24$

1	**2**	**3**	**4**	**5**	**6**	**7**	**8**	**9**	**10**	**11**	**12**	**13**	**14**	**15**	**16**	**17**	**18**	**19**	**20**	**21**	**22**	**23**	**24**
D_1	B_1	D_1	$-B_3$	$-D_3$	B_2	$-D_3$	$-B_1$	D_2	B_3	D_2	$-B_2$	$-D_1$	B_1	$-D_1$	$-B_3$	D_3	B_2	D_3	$-B_1$	D_2	B_3	D_2	$-B_2$

D_1-D_3 are the three drive phases and B_1-B_3 are the three bearing phases, the sign indicates the sense of the winding around the tooth. The q stator teeth are numbered in bold.

D. Bearing Windings of the Exemplary Configuration

To create a resulting radial force, a stator field with the harmonic order equal to the number of rotor pole pairs $p \pm 1$ has to be generated, as explained in Section III-B. Therefore, for the exemplary configuration with an interior rotor the harmonic order of the stator flux density distribution has to be $p + 1 = 14$. With this, the tangential and radial force components sum up in a resulting force pointing in the same desired direction.

The flux density distribution of the bearing system can be calculated analogously to the calculations for the drive system in Section IV-A. The order of the harmonic wave, which is generated by the bearing windings (cf., Table I for the winding scheme sequence), is $c_{2,\mathrm{bng}} = 2$. Using (9), the resulting flux density $\Delta B_{\mathrm{bng}}(\varphi)$ of the bearing windings along the circumferential angle φ can be calculated proportional to

$$\begin{aligned}\Delta B_{\mathrm{bng}}(\varphi)&\sim\sin(12\cdot\varphi)\cdot\sin(2\cdot\varphi)\\&=\frac{\cos(10\cdot\varphi)-\cos(14\cdot\varphi)}{2}.\end{aligned} \tag{11}$$

Therefore, the bearing windings generate the $(p+1)$th harmonic with $f_{\mathrm{bng}}/f_{\mathrm{mech}} = (p + 1) = 14$, which produces, in interaction with the rotor permanent-magnet flux, a resulting radial force acting on the rotor, composed of radial and tangential force components. Fig. 4(b) shows the resulting flux density distribution. Again, the relevant harmonic wave with order $(p + 1)$ is not directly visible, but can be seen in the analytical frequency analysis shown in Fig. 4(d). Fig. 6(b) shows the actual flux distribution gained by 3-D FEM simulations; as one can see, the resulting force consists of radial and tangential force components. The generation of the tangential and radial force components summing up in a resulting force is visible.

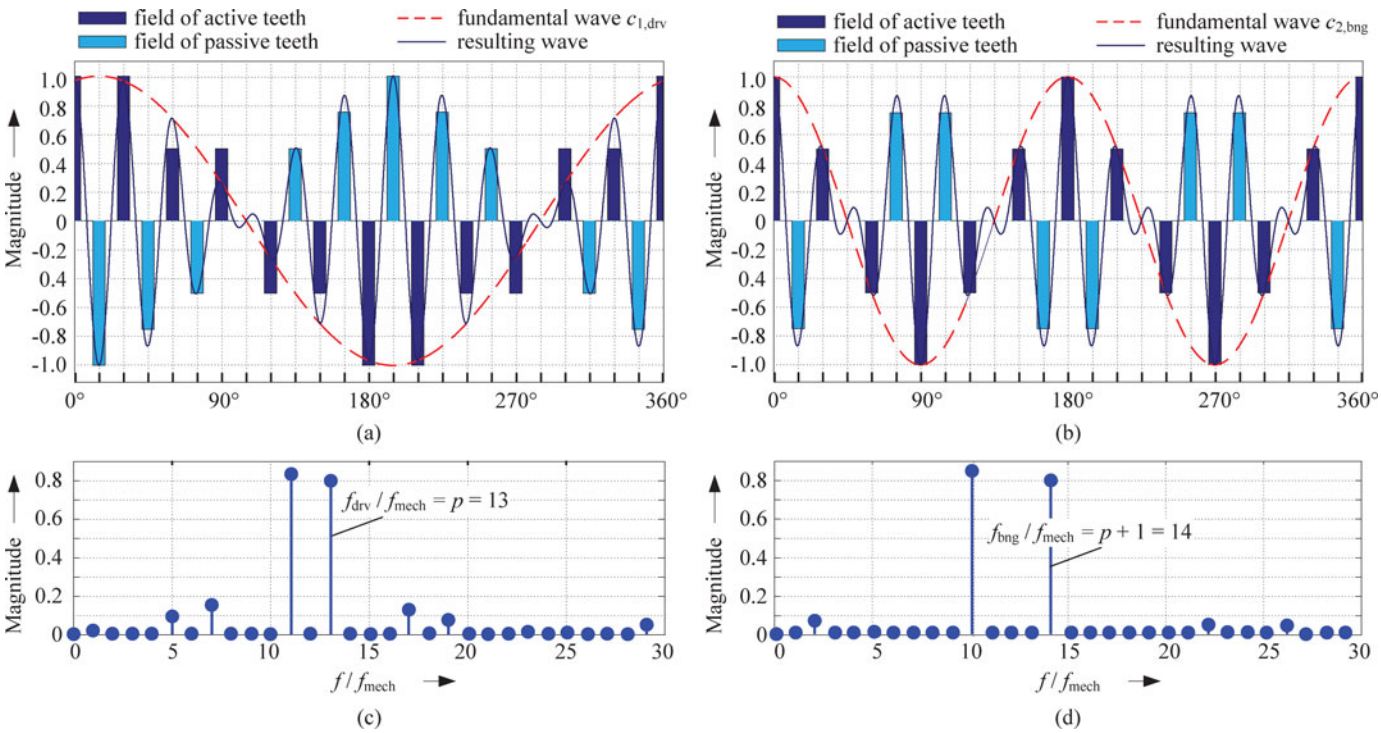

Fig. 4. Flux density distribution in front of the active and passive stator teeth of (a) drive and (b) bearing windings with the corresponding fundamental harmonic waves $c_{1,\mathrm{drv}}$ and $c_{2,\mathrm{bng}}$, respectively, and the harmonic frequency components of the resulting field caused by the windings for (c) drive and (d) bearing.

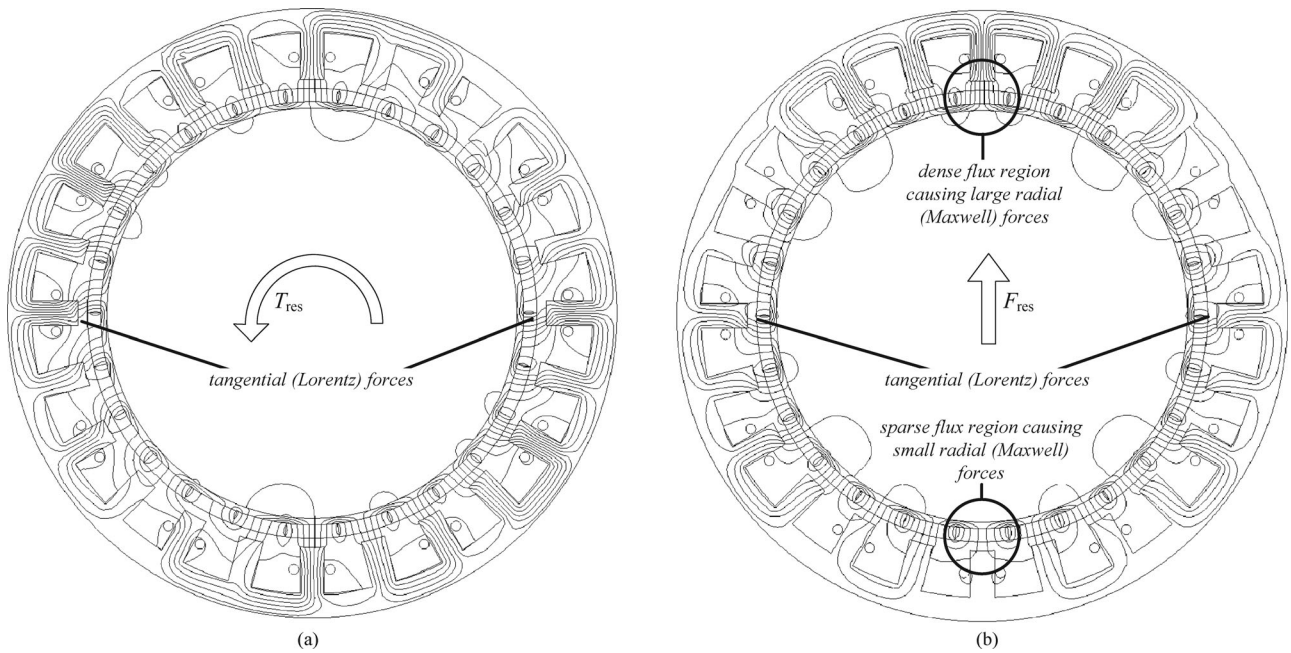

Fig. 5. 3-D FEM simulation results of an exemplary (a) drive and (b) bearing winding excitation resulting in a clockwise torque T_{res}.

V. Influence of the Pole/Slot Combination to the Motor and Bearing Performance

So far, the principles of force and torque generation in bearingless brushless motors have been derived, but no performance criteria have been defined. To find an appropriate combination of the number of rotor poles and stator teeth for a specific application, such criteria help to find the optimal combination.

A. Motor

For the motor part, the achievable torque per ampere winding per phase and tooth has to be maximized, while the cogging torque has to be minimized. According to [25], the total motor torque is given approximately by

$$T_{\mathrm{res}} \approx \frac{1}{4\pi} k_{w,\mathrm{drv}} \cdot N_{\mathrm{drv}} \cdot q \cdot \hat{B}_{\mathrm{pm}} \cdot A_{\delta} \cdot \hat{I} \qquad (12)$$

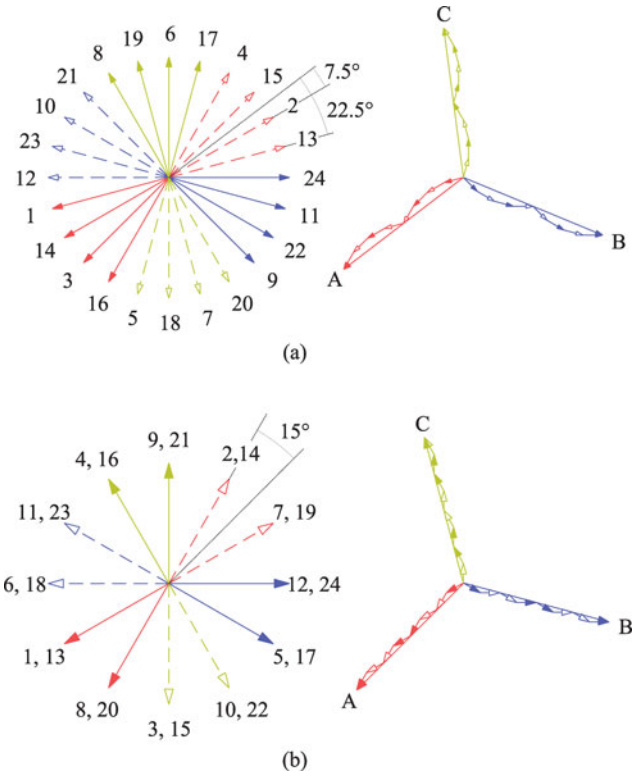

Fig. 6. Derivation of (a) drive winding factor $k_{w,\mathrm{drv}}$ and (b) bearing winding factor $k_{w,\mathrm{bng}}$ with the aid of the star of slots as introduced in [26].

where N_{drv} is the number of turns around each drive tooth, q is the number of teeth, $\hat{\mathrm{B}}_{pm}$ is the peak value of the no-load air-gap flux density, A_δ is the radial rotor surface, $\hat{I}$ is the winding peak current, and $k_{w,\mathrm{drv}}$ is the winding factor of the drive windings. The winding factor describes the percentage of utilization of the current for the motor torque generation. The achievable motor torque is directly proportional to $k_{w,\mathrm{drv}}$, which depends on the combination of $2{\cdot}p$ and q. A winding factor of $k_{w,\mathrm{drv}} = 1$ can be reached if $2{\cdot}p = q$, but this would lead to an unacceptable high cogging torque. For fractional slot motors, $k_{w,\mathrm{drv}}$ is always smaller than 1, since the permanent-magnet flux density can never be perfectly in phase with the stator flux density at each of the $q_{\mathrm{drv}}/m_{\mathrm{drv}}$ stator teeth. Fig. 6(a) shows graphically how the winding factor $k_{w,\mathrm{drv}}$ of the exemplary configuration 26/24 can be derived with the aid of the star of slots, which describes the electrical angles of the electromotive force phasors between the stator slots as introduced in [26]–[28]. The winding factor corresponds to the mean phase shift of the winding currents of a phase and the permanent-magnet flux in front of them as detailed in [26]. For the motor at hand, it can be calculated by

$$k_{w,\mathrm{drv}} = \frac{m_{\mathrm{drv}}}{q_{\mathrm{drv}}} \sum_{i=1}^{q_{\mathrm{drv}}/m_{\mathrm{drv}}} \cos(\Delta\alpha_i) = \frac{1}{4}\left(2 \cdot \cos(22.5^\circ) + 2 \cdot \cos(7.5^\circ)\right) = 0.958 \quad (13)$$

where $\Delta\alpha_i$ is the phase shift between the phasor of the ith drive tooth and the resulting phasor sum of all drive teeth of the corresponding phase.

The cogging torque can be minimized by choosing a combination $2{\cdot}p/q$ with a high least common multiple since this leads to a higher cogging frequency and this lowers the cogging amplitude. If the least common multiple of p and q is orders of magnitude above the number of stator teeth q, the cogging torque can be neglected compared to the motor torque of common motor topologies.

B. Bearing

According to (3), the resulting radial Maxwell force of any two opposite bearing teeth is proportional to

$$\begin{aligned} F_{\mathrm{res1,2}} &= F_{\mathrm{rad,1}} + (-F_{\mathrm{rad,2}}) \\ &\sim (B_{\mathrm{PM}} + \Delta B_{\mathrm{wdg}})^2 - (B_{\mathrm{PM}} - \Delta B_{\mathrm{wdg}})^2 \\ &\sim B_{\mathrm{PM}} \cdot \Delta B_{\mathrm{wdg}} \sim B_{\mathrm{PM}} \cdot I_{\mathrm{wdg}}. \end{aligned} \quad (14)$$

Thus, the resulting force in any direction is proportional to the permanent-magnet flux as well as the flux generated by the bearing winding, which is proportional to the winding current as long as saturation is neglected. Consequently, the resulting overall force is proportional to the winding factor $k_{w,\mathrm{bng}}$, which describes the phase adjustment of the permanent-magnet flux to the bearing winding current. This is true despite the fact that the resulting bearing force consists of tangential and radial forces, i.e., Lorentz and Maxwell forces. Since the bearing force is created by a different harmonic order of the winding compared to the motor winding (14 instead of 13 for the case at hand), the winding factor is different. The winding factor of the bearing winding $k_{w,\mathrm{bng}}$ can be derived graphically as shown in Fig. 8(b) and for the exemplary configuration it can be calculated by

$$k_{w,\mathrm{bng}} = \frac{m_{\mathrm{bng}}}{q_{\mathrm{bng}}} \sum_{i=1}^{q_{\mathrm{bng}}/m_{\mathrm{bng}}} \cos(\Delta\alpha_i) = \frac{1}{4}\left(4 \cdot \cos(15^\circ)\right) = 0.966. \quad (15)$$

C. Winding Factors for Different Configurations

Consequently, not only $k_{w,\mathrm{drv}}$, but also $k_{w,\mathrm{bng}}$ has to be taken into account to reach both a good drive and bearing performance. Together with (1) and (2), a pole/slot combination has to be found, which has a winding factor close to 1 not only for the combination $2{\cdot}p/q$ but also for the combination $2{\cdot}(p+1)/q$ to reach both a good motor and bearing performance.

It can be seen in Table II that the combinations close to the diagonal ($2{\cdot}p/q = 6/6$; 12/12; 18/18; 24/24;. . .) are characterized by very high winding factors (along with low cogging torque). Additionally, the winding factors increase toward higher number of poles and slots. As mentioned earlier, not only the winding factor of the drive winding has to be considered, but also the winding factor of the bearing winding with $p_{\mathrm{bng}} = p_{\mathrm{drv}} + 1$. The exemplary combination with $2{\cdot}p = 26$ and $q = 24$, which was used for the prototype, has superior winding factors (>0.95) for both the motor and bearing winding.

TABLE II
WINDING FACTOR OF THREE-PHASE, SINGLE-LAYER CONFIGURATIONS

	q			
$2{\cdot}p$	6	12	18	24
2	1.000	0.966	0.960	0.958
4	0.866	1.000	0.945	0.966
6			1.000	
8	0.866	0.866	0.617	1.000
10	0.500	0.966	0.735	0.588
12			0.866	
14	0.500	0.966	0.902	0.766
16	0.866	0.866	0.945	0.866
18				
20	0.866	0.500	0.945	0.966
22	0.500	0.259	0.902	0.958
24			0.866	
26	0.500	0.259	0.735	0.958
28	0.866	0.500	0.617	0.966
30			0.500	
32	0.866	0.866	0.328	0.866

The red circles mark the most reasonable combinations of drive and bearing windings for bearingless motors along the line $2{\cdot}p = q$.

TABLE III
COMPARISON OF DIFFERENT CONFIGURATIONS OF $2{\cdot}p/q$

Parameter	$2p = 8$, $q = 6$	$2p = 14$, $q = 12$	$2p = 20$, $q = 18$	$2p = 26$, $q = 24$
Drive winding factor $k_{w,\mathrm{drv}}$	0.866	0.966	0.945	0.958
Drive torque* T_{sim} [mNm/A]	7.27	10.74	10.29	10.31
Cogging torque* T_{cogg} [Nm]	< 0.5	< 0.5	< 0.5	< 0.5
Bearing winding factor $k_{w,\mathrm{bng}}$	0.500	0.866	0.902	0.966
Bearing force* F_{sim} [mN/A]	88	129	152	153

*gained from 3D FEM simulations with optimized geometry parameters for each configuration.

VI. VERIFICATION BY 3-D FEM SIMULATIONS AND EXPERIMENTAL MEASUREMENTS

Table III shows the results of the exemplary configurations $2{\cdot}p/q = 8/6$; 14/12; 20/18; and 26/24 gained by 3-D FEM simulations. Apparently, the combination 26/24 is the best choice in terms of motor torque and levitation force due to the high winding factors, although the improvement seems minor compared to the combination 20/18. The smaller magnet size of the combination 26/24 is a further advantage, as this simplifies the handling and manufacturing of the rotor. The cogging torque of all considered combinations is less than 0.5 Nm and can, therefore, be neglected.

A laboratory prototype with 26 rotor poles and 24 stator slots has been built to verify the assumptions and the simplified model. A photo of the prototype is depicted in Fig. 7, where also the main parts are labeled. With an appropriate control algorithm and a power electronics inverter, the rotor can be levitated contactlessly. The prototype system has been designed for a target maximal rotational speed of 5000 r/min, which is challenging in terms of the bearing control algorithm and signal path requirements due to the high electrical frequencies caused by the high number of rotor pole pairs. In addition, a stable bearing at such high speeds demands very precise position and angular sensors. Experiments with the prototype system have shown that the electrical angle may not differ by more than 15°, which relates to a mechanical angle of $\Delta\varphi_{\mathrm{mech}} = 15°/p = 1.15°$ to guarantee a stable operation of the magnetic

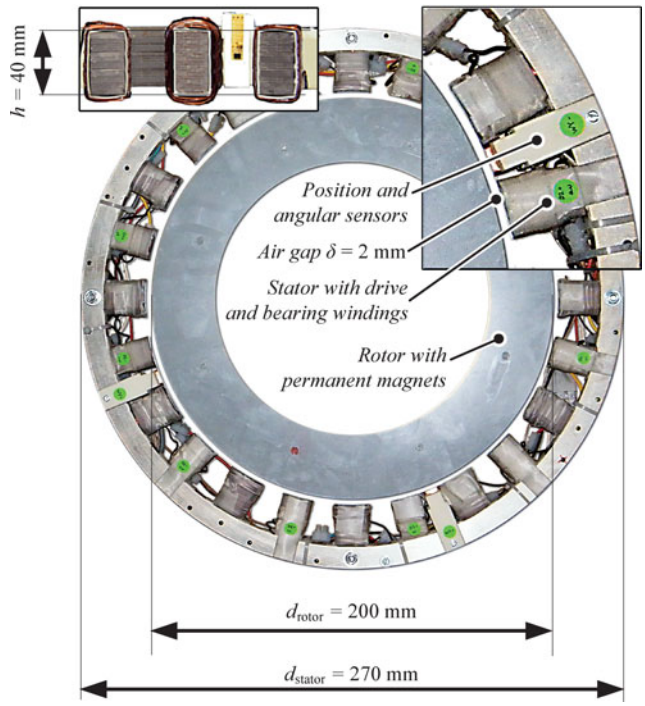

Fig. 7. Photograph of the experimental prototype.

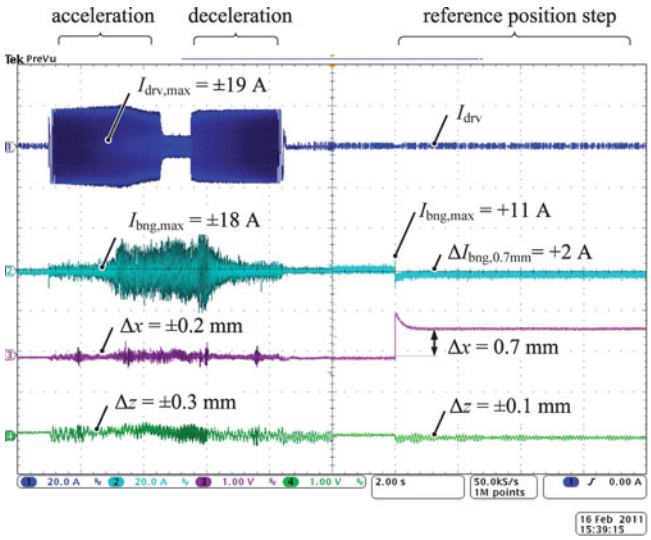

Fig. 8. Experimental results of the prototype: acceleration and deceleration from 0 r/min to 2500 r/min (left), reference position step of $\Delta z = 0.8$ mm (right). CH1: I_{drv} (20 A/div), CH2: I_{bng} (10 A/div), CH3: Δx (1 mm/div), CH4: Δz (1 mm/div).

levitation. This fact results in high demands on the accuracy, the sensitivity, and the noise immunity of the angular sensors. Furthermore, the fabrication of the rotor (including the iron ring and the permanent magnets) must be very precise. While an eventual mass unbalance can be compensated to some degree by mechanical balancing of the rotor, unequally magnetized permanent magnets may lead to high-frequency bearing forces which might be difficult to handle especially for the targeted high rotational speeds.

Fig. 8 shows the drive and bearing currents I_{drv} and I_{bng}, respectively, as well as the radial and axial deflections Δx and

TABLE IV
PROPERTIES AND EXPERIMENTAL RESULTS OF THE PROTOTYPE

Parameter	Symbol	Value	Unit
Number of stator teeth / slots	q	24	
Number of drive teeth	q_{drv}	12	
Number of bearing teeth	q_{bng}	12	
Number of rotor poles	$2{\cdot}p$	26	
Number of bearing phases	m_{bng}	3	
Number drive phases	m_{drv}	3	
Target maximum rotational speed	$n_{r,\max}$	5000	r/min
Permanent magnet length	l_{magnet}	10	mm
Stator iron height	h_{stator}	40	mm
Stator outer diameter	d_{stator}	270	mm
Rotor outer diameter	d_{rotor}	200	mm
Mechanical air-gap	δ	2	mm

Δz, respectively, of the prototype system during controlled operation. The rotor has been accelerated to a maximum speed of $n_r = 2500$ r/min, then decelerated again, and a reference position step has been done during standstill. Further improvements of the power electronics and the sensor system will allow rotational speeds of up to 5000 r/min.

With the laboratory prototype radial suspension, forces up to $F_{\max} = 350$ N in every desired direction can be generated. The most important motor parameters are listed in Table IV.

VII. CONCLUSION

In this paper, the principles of motor torque and suspension force generation in bearingless brushless motors are explained and analyzed.

1) The radial and tangential force components are calculated based on the underlying physical principles.
2) The conditions, which lead to a resulting motor torque and suspension force, respectively, are derived.
3) It is shown how the required stator fields can be generated with an appropriate windings scheme.
4) A performance analysis has been done and a guideline how to choose a configuration, which leads to both a good motor and a good bearing performance, is given.

The general explanations are exemplified and illustrated for an advantageous configuration, and can be used for future developments of bearingless brushless motors with different stator slot/pole-pair combinations. Even an adaption for motors with outer rotors can simply be derived from the presented equations. The results have been verified with a laboratory prototype using the presented exemplary configuration.

REFERENCES

[1] A. Salazar, A. Chiba, and T. Fukao, "A review of development in bearingless motors," in *Proc. 7th Int. Symp. Magn. Bearings*, Zurich, Switzerland, Aug. 23–25, 2000, pp. 335–340.

[2] J. Zhou and K. Tseng, "A disk-type bearingless motor for use as satellite momentum-reaction wheel," in *Proc. 33rd Annu. IEEE Power Electron. Spec. Conf.*, 2002, pp. 1971–1975.

[3] Y. Chisti and M. Moo-Young, "Clean-in-place systems for industrial bioreactors: Design, validation and operation," *J. Ind. Microbiol. Biotechnol.*, vol. 13, pp. 201–207, Jul. 1994.

[4] S. Yang and M. Huang, "Design and implementation of a magnetically levitated single-axis controlled axial blood pump," *IEEE Trans. Ind. Electron.*, vol. 56, no. 6, pp. 2213–2219, Jun. 2009.

[5] Y. Okada, N. Yamashiro, K. Ohmori, T. Masuzawa, T. Yamane, Y. Konishi, and S. Ueno, "Mixed flow artificial heart pump with axial self-bearing motor," *IEEE/ASME Trans. Mechatronics*, vol. 10, no. 6, pp. 658–665, Dec. 2005.

[6] M. Ooshima, S. Kitazawa, A. Chiba, T. Fukao, and D. Dorrell, "Design and analyses of a coreless-stator-type bearingless motor/generator for clean energy generation and storage systems," *IEEE Trans. Magn.*, vol. 42, no. 10, pp. 3461–3463, Oct. 2006.

[7] C. Weisbacher, H. Stelzer, and K. Hameyer, "Application of a tubular linear actuator as an axial magnetic bearing," *IEEE/ASME Trans. Mechatronics*, vol. 15, no. 4, pp. 615–622, Aug. 2010.

[8] S.-L. Chen and C.-C. Weng, "Robust control of a voltage-controlled three-pole active magnetic bearing system," *IEEE/ASME Trans. Mechatronics*, vol. 15, no. 3, pp. 381–388, Jun. 2010.

[9] K. Komori and T. Yamane, "Magnetically levitated micro PM motors by two types of active magnetic bearings," *IEEE/ASME Trans. Mechatronics*, vol. 6, no. 1, pp. 43–49, Mar. 2001.

[10] T. Schneeberger, T. Nussbaumer, and J. W. Kolar, "Magnetically levitated homopolar hollow-shaft motor," *IEEE/ASME Trans. Mechatronics*, vol. 15, no. 1, pp. 97–107, Feb. 2010.

[11] S. Zhang and F. L. Luo, "Direct control of radial displacement for bearingless permanent-magnet-type synchronous motors," *IEEE Trans. Ind. Electron.*, vol. 56, no. 2, pp. 542–552, Feb. 2009.

[12] J. Sun, Q. Zhan, and L. Liu, "Modelling and control of bearingless switched reluctance motor based on artificial neural network," in *Proc. 31st Annu. Conf. IEEE Ind. Electron. Soc.*, 2005, pp. 1638–1643.

[13] T. Tera, Y. Yamauchi, A. Chiba, T. Fukao, and M. Rahman, "Performances of bearingless and sensorless induction motor drive based on mutual inductances and rotor displacements estimation," *IEEE Trans. Ind. Electron.*, vol. 53, no. 1, pp. 187–194, Feb. 2005.

[14] P. Karutz, T. Nussbaumer, W. Gruber, and J. W. Kolar, "Novel magnetically levitated two-level motor," *IEEE/ASME Trans. Mechatronics*, vol. 13, no. 6, pp. 658–668, Dec. 2008.

[15] Q. Nguyen and S. Ueno, "Modeling and control of salient-pole permanent magnet axial-gap self-bearing motor," *IEEE/ASME Trans. Mechatronics*, vol. 16, no. 3, pp. 518–526, Jun. 2011.

[16] K. Asami, A. Chiba, M. Rahman, T. Hoshino, and A. Nakajima, "Stiffness analysis of a magnetically suspended bearingless motor with permanent magnet passive positioning," *IEEE Trans. Ind. Electron.*, vol. 41, no. 10, pp. 3820–3822, Oct. 2005.

[17] S.-H. Park and C.-W. Lee, "Decoupled control of a disk-type rotor equipped with a three-pole hybrid magnetic bearing," *IEEE/ASME Trans. Mechatronics*, vol. 15, no. 5, pp. 793–804, Oct. 2010.

[18] F. Zürcher, T. Nussbaumer, W. Gruber, and J. W. Kolar, "Design and development of a 26-pole and 24-slot bearingless motor," *IEEE Trans. Magn.*, vol. 45, no. 10, pp. 4594–4597, Oct. 2009.

[19] S. Silber, W. Amrhein, P. Bosch, R. Schöb, and N. Barletta, "Design aspects of bearingless slice motors," *IEEE/ASME Trans. Mechatronics*, vol. 10, no. 6, pp. 611–617, Dec. 2005.

[20] H. Grabner, W. Amrhein, S. Silber, and W. Gruber, "Nonlinear feedback control of a bearingless brushless DC motor," *IEEE/ASME Trans. Mechatronics*, vol. 15, no. 1, pp. 40–47, Feb. 2010.

[21] T. Tera, Y. Yamauchi, A. Chiba, T. Fukao, and M. A. Rahman, "Performances of bearingless and sensorless induction motor drive based on mutual inductances and rotor displacements estimation," *IEEE Trans Ind. Electron.*, vol. 53, no. 1, pp. 187–194, Feb. 2006.

[22] L. Xianxing, W. Wei, and Z. Damin, "Direct torque control system using space vector modulation for bearingless induction motor based on active disturbance rejection controller," in *Proc. 29th Chinese Control Conf.*, Jul. 29–31, 2010, pp. 3311–3315.

[23] Q. Hijikata, S. Kobayashi, M. Takemoto, Y. Tanaka, A. Chiba, and T. Fukao, "Basic characteristics of an active thrust magnetic bearing with a cylindrical rotor core," *IEEE Trans. Magn.*, vol. 44, no. 12, pp. 4167–4170, Dec. 2008.

[24] K. Küpfmüller, *Einführung in die theoretische Elektrotechnik*. 14. Auflage, Berlin, Germany: Springer-Verlag, 1993, p. 332.

[25] F. Magnussen and C. Sadarangani, "Winding factors and Joule losses of permanent magnet machines with concentrated windings," in *Proc. IEEE Int. Electr. Mach. Drives Conf.*, Jun. 1–4, 2003, vol. 1, pp. 333–339.

[26] N. Bianchi and M. D. Pre, "Use of the star of slots in designing fractional-slot single-layer synchronous motors," *IEE Proc.—Electric Power Appl.*, vol. 153, no. 3, pp. 459–466, May 2006.

[27] J. T. Chen and Z. Q. Zhu, "Winding configurations and optimal stator and rotor pole combination of flux-switching PM brushless AC machines," *IEEE Trans. Energy Conversion*, vol. 25, no. 2, pp. 293–302, Jun. 2010.

[28] S. B. Ozturk and H. A. Toliyat, "Direct torque and indirect flux control of brushless DC motor," *IEEE/ASME Trans. Mechatronics.*, vol. 16, no. 2, pp. 351–360, Apr. 2011.

Franz Zürcher (S'08) received the M.Sc. degree in electrical engineering from the Swiss Federal Institute of Technology (ETH) Zurich, Zurich, Switzerland, in 2007, where he focused on mechatronics, power electronics, and microelectronics. During his M.Sc. studies, he designed and realized a 1.5-kW converter for bearingless motors in cooperation with Levitronix GmbH. Since 2008, he has been working toward the Ph.D. degree in the Power Electronic Systems Laboratory, ETH Zurich, where he is currently involved in research on high-acceleration magnetically levitated motors.

Thomas Nussbaumer (S'02–M'06) was born in Vienna, Austria, in 1975. He received the M.Sc. degree (Hons.) in electrical engineering from the University of Technology Vienna, Vienna, in 2001, and the Ph.D. degree from the Power Electronic Systems (PES) Laboratory, Swiss Federal Institute of Technology (ETH) Zurich, Zurich, Switzerland, in 2004.

From 2001 to 2006, he was with the PES, where he was involved in research on modeling, design, and control of three-phase rectifiers, power factor correction techniques, and electromagnetic compatibility. Since 2006, he has been with Levitronix GmbH, Zurich, where he is currently involved in research on bearingless motors, magnetic levitation, and permanent-magnet motor drives for the semiconductor and biotechnology industry. His current research is focused on compact and high-performance mechatronic systems including novel power electronics topologies, control techniques, drive systems, sensor technologies, electromagnetic interference, and thermal aspects.

Johann W. Kolar (M'89–SM'04–F'10) received the Ph.D. degree (*summa cum laude/promotio sub auspiciis praesidentis rei publicae*) from the University of Technology Vienna, Vienna, Austria.

Since 1984, he has been working as an Independent International Consultant in close collaboration with the University of Technology Vienna, in the fields of power electronics, industrial electronics, and high-performance drives. He has proposed numerous novel PWM converter topologies, and modulation and control concepts, e.g., the VIENNA rectifier and the three-phase ac–ac sparse matrix converter. He has published more than 300 scientific papers in international journals and conference proceedings and has filed more than 75 patents. He joined the Power Electronic Systems Laboratory, Swiss Federal Institute of Technology (ETH) Zurich, on February 1, 2001. His current research interests include ac–ac and ac–dc converter topologies with low effects on the mains, e.g., for power supply of telecommunication systems, More-Electric-Aircraft and distributed power systems in connection with fuel cells. Further main areas are the realization of ultracompact intelligent converter modules employing latest power semiconductor technology (SiC), novel concepts for cooling and EMI filtering, multidomain/multiscale modeling and simulation, pulsed power, bearingless motors, and power MEMS.

Dr. Kolar received the Best Transactions Paper Award of the IEEE Industrial Electronics Society in 2005. He also received an Erskine Fellowship from the University of Canterbury, New Zealand, in 2003. In 2006, the European Power Supplies Manufacturers Association (EPSMA) awarded the Power Electronics Systems Laboratory of ETH Zurich as the leading academic research institution in Europe. He is a member of the Institute of Electrical Engineers of Japan and of Technical Program Committees of numerous international conferences in the field (e.g., Director of the Power Quality Branch of the International Conference on Power Conversion and Intelligent Motion). From 1997 through 2000, he was an Associate Editor of the IEEE TRANSACTIONS ON INDUSTRIAL ELECTRONICS and since 2001 he has been an Associate Editor of the IEEE TRANSACTIONS ON POWER ELECTRONICS. Since 2002, he has also been an Associate Editor of the *Journal of Power Electronics* of the Korean Institute of Power Electronics and a member of the Editorial Advisory Board of the *IEEJ Transactions on Electrical and Electronic Engineering*.